Introduction to Suomi national polar-orbiting partnership advanced technology microwave sounder for numerical weather prediction and tropical cyclone applications

F. Weng,[1] X. Zou,[2] X. Wang,[3] S. Yang,[3] and M. D. Goldberg[4]

Received 20 May 2012; revised 27 July 2012; accepted 25 August 2012; published 6 October 2012.

[1] The Suomi National Polar-orbiting Partnership (NPP) satellite was successfully launched on 28 October 2011. On board the Suomi NPP, the Advanced Technology Microwave Sounder (ATMS) is a cross-track scanning instrument and has 22 channels at frequencies ranging from 23 to 183 GHz which allows for probing the atmospheric temperature and moisture under clear and cloudy conditions. ATMS inherited most of the sounding channels from its predecessors: Advanced Microwave Sounding Unit-A (AMSU-A) and Microwave Humidity Sounder (MHS) onboard NOAA and MetOp satellites. However, ATMS has a wider scan swath and has no gaps between two consecutive orbits. It includes one new temperature sounding channel and two water vapor sounding channels and provides more details of thermal structures in lower troposphere, especially for the storm conditions such as tropical cyclones. While ATMS temperature sounding channels have shorter integration time and therefore higher noise than AMSU-A, the ATMS observations from their overlapping field of views are resampled to produce AMSU-A-like measurements.

Citation: Weng, F., X. Zou, X. Wang, S. Yang, and M. D. Goldberg (2012), Introduction to Suomi national polar-orbiting partnership advanced technology microwave sounder for numerical weather prediction and tropical cyclone applications, *J. Geophys. Res.*, *117*, D19112, doi:10.1029/2012JD018144.

1. Introduction

[2] On 28 October 2011, the Suomi National Polar-orbiting Partnership (NPP) satellite was successfully launched into a circular, near-polar, afternoon-configured (1:30 P.M. ±10 minutes) orbit with an altitude of 824 km above the Earth and an inclination angle of 98.7 ± 0.05° to the Equator. It is the pathfinder for the Joint Polar Satellite System (JPSS) operational satellite series. The major objectives of the Suomi NPP satellite are (1) to provide a continuation of a group of Earth system observations initiated by the Earth Observing System Terra, Aqua, and Aura missions; and (2) to provide preoperational risk reduction, demonstration, and validation for selected JPSS instruments and ground processing data systems for the operational forecasting community. The Advanced Technology Microwave Sounder (ATMS) onboard Suomi NPP operates in conjunction with the Cross-Track Infrared Sounder (CrIS) to profile atmospheric temperature and moisture in clear-sky and cloudy conditions except for heavy precipitation where the microwave sounding capability is degraded by the scattering signatures from large raindrops and ice particles. Together, ATMS and CrIS will support a continuing advance in numerical weather prediction (NWP) for improved short- to medium-range weather forecast skills.

[3] ATMS calibration data, including raw data, geolocation, telemetry and house-keeping data, have been fully processed at the NPP Interface Data and Processing Segment (IDPS) since the Suomi NPP launch. At the ATMS panel review held on 13 January 2012, it was concluded that the ATMS data reached its beta version. Through more intensive calibration efforts, the TDR data is close to the provision version and can be used by the user community for various applications. The ATMS antenna temperature data record (TDR) and sensor data record (SDR) radiances are now being distributed to the user community from NOAA's Comprehensive Large Array-Data Stewardship Systems (CLASS).

[4] This work describes the ATMS data precision, channel characteristics, and new field-of-view (FOV) features. In this study, the ATMS instrument characteristics are first presented. Cloud liquid water path (LWP) derived from

[1]Center for Satellite Applications and Research, National Environmental Satellite, Data, and Information Service, NOAA, College Park, Maryland, USA.
[2]Department of Earth, Ocean, and Atmospheric Science, Florida State University, Tallahassee, Florida, USA.
[3]Center of Data Assimilation for Research and Application, Nanjing University of Information Science and Technology, Nanjing, China.
[4]Joint Polar Satellite System Program Office, NOAA, Silver Spring, Maryland, USA.

Corresponding author: F. Weng, Center for Satellite Applications and Research, National Environmental Satellite, Data, and Information Service, NOAA, 5830 University Research Ct., College Park MD 20740, USA. (fuzhong.weng@noaa.gov)

Table 1. Channel Characteristics of ATMS and AMSU[a]

Channel		Frequency (GHz)		NEΔT (K)		Beam Width (deg)		Peak WF (hPa)
ATMS	AMSU	ATMS	AMSU	ATMS	AMSU	ATMS	AMSU	ATMS or AMSU
1		23.8		0.50	0.30	5.2	3.3	Window
2		31.4		0.60	0.30	5.2	3.3	Window
3		50.3		0.70	0.40	2.2	3.3	Window
4		51.76		0.50		2.2		950
5	4	52.8		0.50	0.25	2.2	3.3	850
6	5	53.596 $\pm$ 0.115		0.50	0.25	2.2	3.3	700
7	6	54.4		0.50	0.25	2.2	3.3	400
8	7	54.94		0.50	0.25	2.2	3.3	250
9	8	55.5		0.50	0.25	2.2	3.3	200
10	9	57.29		0.75	0.25	2.2	3.3	100
11	10	57.29 $\pm$ 0.217		1.00	0.40	2.2	3.3	50
12	11	57.29 $\pm$ 0.322 $\pm$ 0.048		1.00	0.40	2.2	3.3	25
13	12	57.29 $\pm$ 0.322 $\pm$ 0.022		1.25	0.60	2.2	3.3	10
14	13	57.29 $\pm$ 0.322 $\pm$ 0.010		2.20	0.80	2.2	3.3	5
15	14	57.29 $\pm$ 0.322 $\pm$ 0.0045		3.60	1.20	2.2	3.3	2
16	15	88.2	89.0	0.30	0.50	2.2	3.3	Window
	16		89.0	0.60	0.84	1.1	1.1	Window
17	17	165.5	157.0					Window
18	20	183.31 $\pm$ 7.0	190.31	0.80	0.84	1.1	1.1	800
19		183.31 $\pm$ 4.5		0.80	0.60	1.1	1.1	700
20	19	183.31 $\pm$ 3.0		0.80	0.70	1.1	1.1	500
21		183.31 $\pm$ 1.8		0.80	1.06	1.1	1.1	400
22	18	183.31 $\pm$ 1.0		0.90		1.1		300

[a]In AMSU column, MHS channels 16 to 20 are also included. The peak weight function (WF) is also indicated.

ATMS is compared with LWP from AMSU-A from NOAA-18. Scan-dependent biases of ATMS TDR data at midlevel and upper level sounding channels is examined over oceans under clear-sky conditions. Also, the information content from the full suite of ATMS sounding channels is compared with that from the AMSU-A/MHS-like channels within and around a tropical cyclone. More studies on ATMS calibration and validation (CalVal) will be followed through a series of science papers from the ATMS CalVal team members.

2. A Brief Description of ATMS Instrument Characteristics

[5] ATMS is a total power radiometer and scans in a cross-track manner within $\pm 52.7^\circ$ with respect to the nadir direction. It has a total of 22 channels with the first 16 channels primarily for temperature soundings from the surface to about 1 hPa ($\sim$45 km) and the remaining channels for humidity soundings in the troposphere from the surface to about 200 hPa ($\sim$10 km). There are two receiving antennas: one serving channels 1–15 below 60 GHz, and the other for channels above 60 GHz. Table 1 provides a comparison of channel characteristics between ATMS onboard Suomi NPP and AMSU-A/MHS (to be referred AMSU hereafter for simplicity) onboard NOAA-18, -19 and MetOp-A. ATMS has 22 channels while AMSU has 20 channels. Seventeen of ATMS channels (ATMS channels 1–3, 5–15, 17, 20 and 22) have the same frequencies as its predecessor AMSU (AMSU channels 1–14, 16–19), two ATMS channels (ATMS channels 16 and 18) have slightly different frequencies from AMSU channels (AMSU channels 15 and 20), and three new ATMS channels (ATMS channels 4, 19 and 21) are added. The ATMS channel 4 is new with its central frequency located at 51.76 GHz and contains temperature information in the lower troposphere that is much needed for NWP. The ATMS channels 19 and 21 are also new with their central frequencies located near 183-GHz water vapor absorption line (e.g., channel 19 at 183.31 $\pm$ 4.5 GHz and channel 21 at 183.31 $\pm$ 1.8 GHz) and are added for better profiling atmospheric moisture.

[6] The ATMS instrument noise is fully characterized during the period of the prelaunch and on-orbit calibration and is shown in Figure 1. In general, the ATMS noise equivalent differential temperature (NEDT) for temperature sounding channels is higher than the AMSU-A values mainly because the ATMS sampling time (e.g., the effective integration time for each FOV) is much shorter than that of AMSU-A. Specifically, The integration time (e.g., the FOV stepping time) for all ATMS channels is 18 ms, while that for AMSU-A channels 1–2 and 3–15 is 165 ms and 158 ms, respectively. However, NEDTs derived from the prelaunch and on-orbit calibration are much smaller than the specification, and in particular the postlaunch ATMS instrument noise is close to the AMSU-A values for its temperature sounding channels except for upper stratospheric channels. For user communities who continue their AMSU-A-like applications with ATMS, the ATMS data remapped into the same resolution as the AMSU-A are also available from CLASS. The Backus-Gilbert method [*Backus and Gilbert*, 1968] was used for the conversion from ATMS FOVs to AMSU-A FOVs. This method provides not only an optimal combination of measurements for determining the average brightness temperature within a specified region, but also a quantitative measure of the tradeoff between resolution and noise. More details on B-G method and its applications can be found in *Stogryn* [1978], *Kirsch et al.* [1988], and *Poe* [1990].

[7] Figure 2 shows the weighting functions for the 22 ATMS channels calculated by the Community Radiative Transfer Model (CRTM) developed by the U.S. Joint Center for Satellite Data Assimilation (JCSDA) [*Weng*, 2007; *Han et al.*, 2007]. It is seen that ATMS channels 1–16 profile

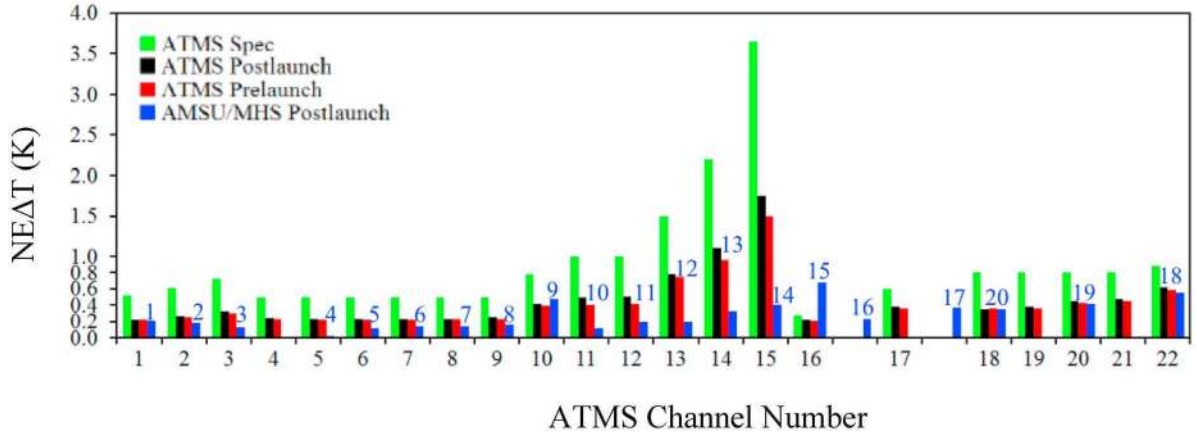

Figure 1. ATMS Noise Equivalent Differential Temperature (NEDT) in comparison with AMSU-A/MHS. The ATMS channel number is indicated on the *x* axis and the AMSU channel number is indicated in the figure in blue.

the atmospheric temperature from the surface to 0.1 hPa and ATMS channels 17–22 profile the water vapor in the troposphere. ATMS channels 1–4 and 16–17 are near the atmospheric absorption window and are affected by the radiation from both the Earth's surface and the atmosphere. Table 2 provides an estimate of the atmospheric contributions to the total radiation calculated using the U.S. standard profile. The surface radiation contributes about 89%, 94% and 65% for ATMS channels 1–3 (see Table 2). The newly added ATMS channel 4 has more radiation contribution from the atmosphere (e.g., 51%) than surface channels 1–3.

[8] The beam width for AMSU channels 1–15 and 16–20 is 3.3° and 1.1°, respectively. The ATMS channels 3–16 have a beam width of 2.2°, which is smaller than AMSU temperature channels 1–15. However, the beam width for ATMS surface channels 1–2 is 5.2°, which is much larger than the corresponding AMSU channels 1–2. The six of seven ATMS channels above 60 GHz, channels 17–22, have a beam width of 1.1°, which is the same as AMSU water vapor channels 16–20.

[9] The above mentioned differences of the beam width between ATMS and AMSU channels, along with the difference of satellite altitudes between Suomi NPP (824 km) and its predecessors such as NOAA-19 (870 km), result in significant differences in FOV sizes between ATMS and AMSU (see Figure 3). The largest FOV difference between ATMS and AMSU is in ATMS/AMSU channels 1–2 (Figure 3, top). A single ATMS FOV is about 1.6 of the AMSU FOV in diameter, which is mostly determined by beam width differences between the two instruments. There is no overlap between the neighboring FOVs neither between the neighboring scanlines of AMSU, but significant overlaps occur for ATMS FOVs and

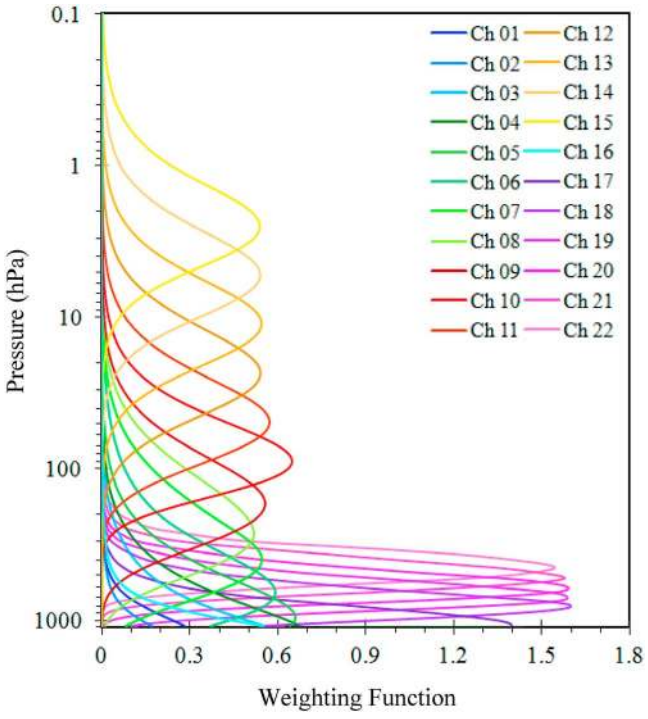

Figure 2. Weighting functions for the 22 ATMS channels.

Table 2. Atmospheric Contributions to the Total Radiation at the Top of Atmosphere (Unit: 100%)

Channel	Atmospheric Contribution
1	0.11
2	0.06
3	0.35
4	0.51
5	0.72
6	0.89
7	0.97
8	0.98
9	0.99
10	0.99
11	0.99
12	0.99
13	1.00
14	1.00
15	1.00
16	0.18
17	0.58
18	0.94
19	0.98
20	0.99
21	0.99
22	0.99

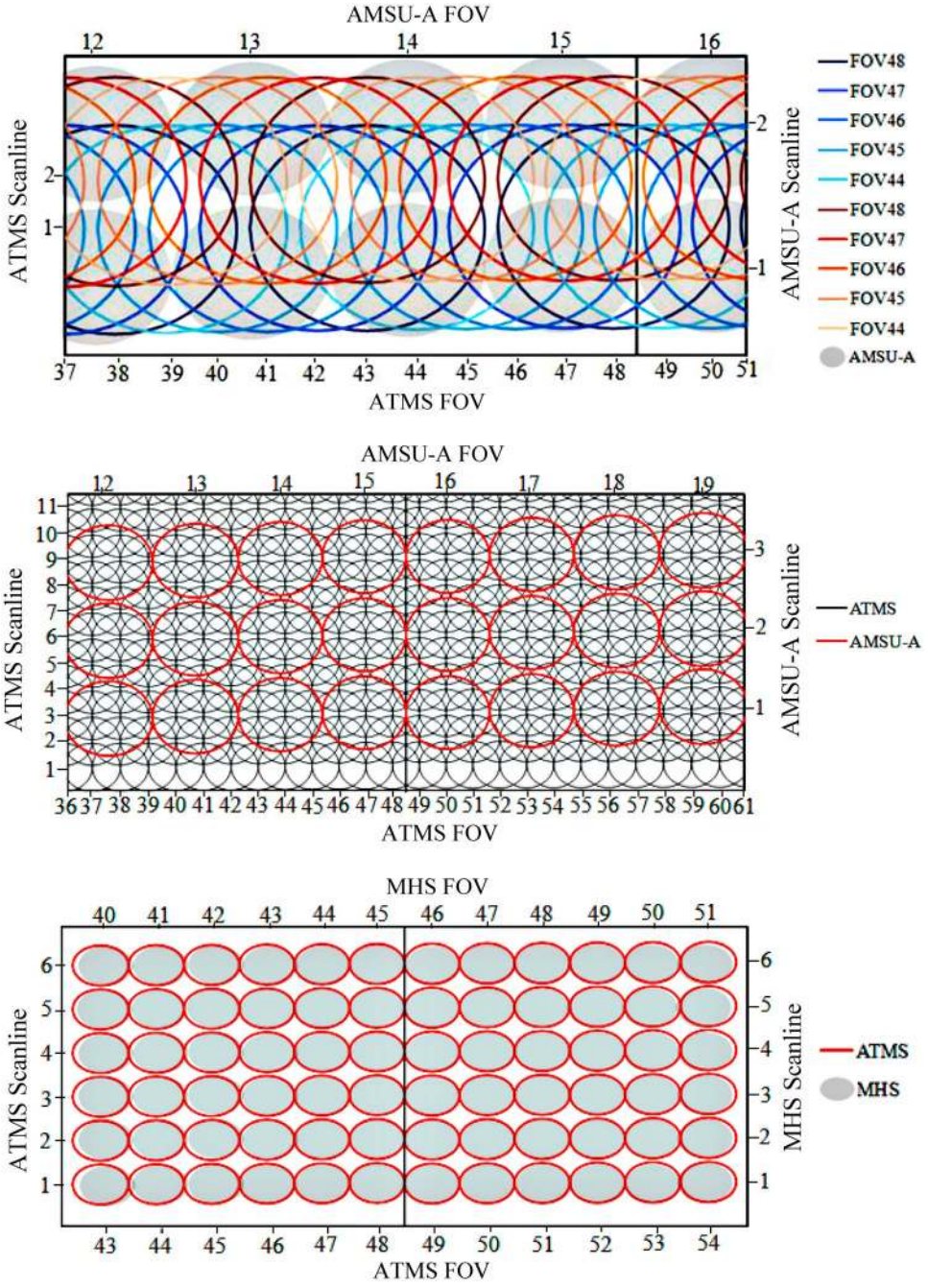

Figure 3. FOVs for ATMS (top) channels 1–2 with ATMS beam width 5.2°, (middle) channels 3–16 with beam width 2.2°, and (bottom) channels 17–22 with beam width 1.1°. The FOVS for AMSU-A and MHS onboard NOAA-18 are also shown.

scanlines of channels 1–2. For example, the FOV48 has overlaps with the neighboring four FOVs and four scanlines.

[10] A single AMSU FOV for channels 3–15 is about 1.5 times larger than that of ATMS channels 3–16. At these channels, a single ATMS FOV overlaps with its surrounding four FOVs. The differences of FOVs for water vapor channels between ATMS and AMSU are rather small. There is a small difference in integration time between ATMS (18 ms) and MHS (19 ms).

[11] The oversampling features of ATMS will allow for an estimation of brightness temperatures at resolutions higher or lower than the raw ATMS data resolution. However, an optimal balance between desirable resolution and the resulting data noise must be taken into consideration when developing such an estimate for investigating specific weather systems.

3. Bias Characterization

[12] An important application of ATMS data is for improving NWP forecast skill through data assimilation. All data assimilation methods employ either a maximum

likelihood estimate or minimum variance estimate under the assumption that both observations and models are unbiased. Any bias related to the instrument and forward modeling must be quantified and removed in satellite data assimilation. Since the weighted differences between observations and model simulations, $O - B$, are minimized in satellite data assimilation, the observation bias (μ^o) and model bias (μ^b), can be lumped together as follows:

$$(O - \mu^o) - (B - \mu^b) = O - B - (\mu^o + \mu^b). \quad (1)$$

[13] Therefore, $O - B$ statistics can be used to estimate the sum of observation and model biases $\mu^o + \mu^b$.

[14] An assessment of the ATMS data biases requires a forward radiative transfer model for calculating the microwave radiation at 22 ATMS frequencies at the top of the atmosphere for any given atmospheric state (e.g., temperature and water vapor profiles) and the Earth's surface properties (e.g., surface temperature, surface emissivity, surface wind speed, etc.). In this study, the CRTM and National Center for Environmental Prediction (NCEP) global forecast system (GFS) 6-h forecasts are used for bias characterization. The NCEP GFS 6-h forecast fields have a horizontal resolution $0.3125^\circ \times 0.3125^\circ$ and 64 vertical levels. The highest vertical level is around 0.01 hPa.

[15] Brightness temperatures simulated by CRTM using NWP analysis/forecast fields are most accurate for sounding channels in clear-sky conditions over oceans. In this study, ATMS observations in clear-sky condition during 20–27 December 2011 are used for characterizing the performance of the ATMS temperature-sounding channels 5–15. To detect a cloud-affected ATMS FOV measurement, an algorithm, similar to that developed by *Weng et al.* [2003] for AMSU-A, is used for retrieving atmospheric cloud liquid water path (LWP) from ATMS channels 1 and 2 measurements. As demonstrated, microwave measurements at lower-frequency window channels can be directly related to LWP and water vapor path (WVP) through an emission-based radiative transfer model [*Greenwald et al.*, 1993; *Weng and Grody*, 1994, 2000; *Weng et al.*, 1997; *Wentz*, 1997; *Grody et al.*, 2001; *Weng et al.*, 2003]. The effects of surface parameters such as emissivity and temperature on the measurements at two ATMS channels are taken into account from GFS forecast fields. Specifically, cloud LWP can be derived by the following formula:

$$LWP = a_0\mu\left[\ln\left(T_s - T_b^{Ch2}\right) - a_1\ln\left(T_s - T_b^{Ch1}\right) - a_2\right] \quad (2)$$

where coefficients a_0, a_1, and a_2 are calculated by

$$a_0 = -0.5\kappa_\nu^{Ch1}/\left(\kappa_\nu^{Ch1}\kappa_l^{Ch2} - \kappa_\nu^{Ch2}\kappa_l^{Ch1}\right)$$
$$a_1 = \kappa_\nu^{Ch2}/\kappa_\nu^{Ch2}$$
$$a_2 = -2.0\left(\tau_0^{Ch2} - a_1\tau_0^{Ch1}\right)/\mu + (1.0 - a_1)\ln(T_s) + \ln\left(1.0 - \varepsilon^{Ch2}\right) - a_1\ln\left(1.0 - \varepsilon^{Ch1}\right)$$

with T_b^{Ch1} and T_b^{Ch2} representing brightness temperatures at 23.8 and 31.4 GHz, respectively, T_s is the sea surface temperature (SST), κ_ν is the water vapor mass absorption coefficient, κ_l is cloud liquid water the mass absorption coefficient, τ_o is the optical thickness, ε is the surface emissivity, and $\mu = \cos\theta$, where θ is the satellite zenith angle.

[16] The cloud LWP at different scan angle (α) is calculated using (2). It is useful to recall that there is a one-to-one relationship between the satellite zenith angle (θ) and scan angle (α): $\sin(\theta) = (R + H)\sin\alpha/R$, where H is the altitude of the Suomi NPP satellite and R is the Earth radius. The limb effects for the cross-tracking scanning ATMS are automatically taken cared of by the factor μ in (2).

[17] Figure 4 presents the global distributions of brightness temperatures at channels 1 and 2 from ATMS and AMSU-A (Figures 4a–4d) as well as the LWP retrievals derived from these two channels using (1) for the ascending nodes on 20 December 2011. The sensitivity of these two window channels to the Earth's surface (e.g., surface emissivity and surface skin temperature) gives a sharp contrast between land and ocean. Due to much large surface emission, brightness temperatures over land are higher than those than over ocean. The relative contribution of the atmospheric absorption to the total radiance over ocean is thus higher than that over land, leading to a stronger scan-dependence of the brightness temperatures over ocean than over land. The global LWP distribution deduced from ATMS (Figure 4e) compares favorably with the AMSU-A derived LWP (Figure 4f). The ATMS provides a nearly continuous distribution of global LWP while AMSU-A has large orbital gaps in low latitudes. Spatial features of large LWP (Figures 4e and 4f) can be seen in the global distribution of brightness temperature of channel 2 (Figures 4c and 4d), which is the primary channel for the LWP retrieval. Channel 1 is most sensitive to atmospheric water vapor path, which is usually high over cloudy areas.

[18] An LWP of 0.05 kg/m^2 is used as a threshold for detecting cloud-affected ATMS sounding channels. An ATMS sounding channel corresponding to the LWP less than this threshold is treated clear FOV [*Weng et al.*, 1997]. During the study period, there are more than 250 data counts within any $1^\circ \times 1^\circ$ grid boxes over the globe.

[19] Differences between ATMS data and its predecessor AMSU-A could be inferred from the differences between ATMS raw and remapped data. The differences of observation resolutions between ATMS raw and remapped data are first examined (Figure 5). The ATMS FOV diameter at nadir is 31.6, while that of the remapped data FOV is 48.6 km. The cross-track FOV size increases much rapidly than that in along-track direction. The differences of along-track FOV size between the raw and remapped ATMS TDR remains nearly constant with respect to scan angle, while the size differences of cross-track FOVs between the raw and remapped data decreases with the increase of scan angle. The cross-track and along-track FOV sizes of ATMS at the largest scan angle (e.g., $\pm 52.77^\circ$) are 136.7 km and 60 km, respectively, while those of the remapped one at the largest scan angle (e.g., $\pm 48.33^\circ$) are 155.2 km and 85.6 km, respectively.

[20] ATMS remapped data is a weighted average of the ATMS raw data. Differences in observational resolutions between ATMS raw and remapped data change the dynamic ranges and standard deviations of differences between observations and model simulations (O-B). The scatterplots of the temperature dependence of O-B for ATMS channel 6

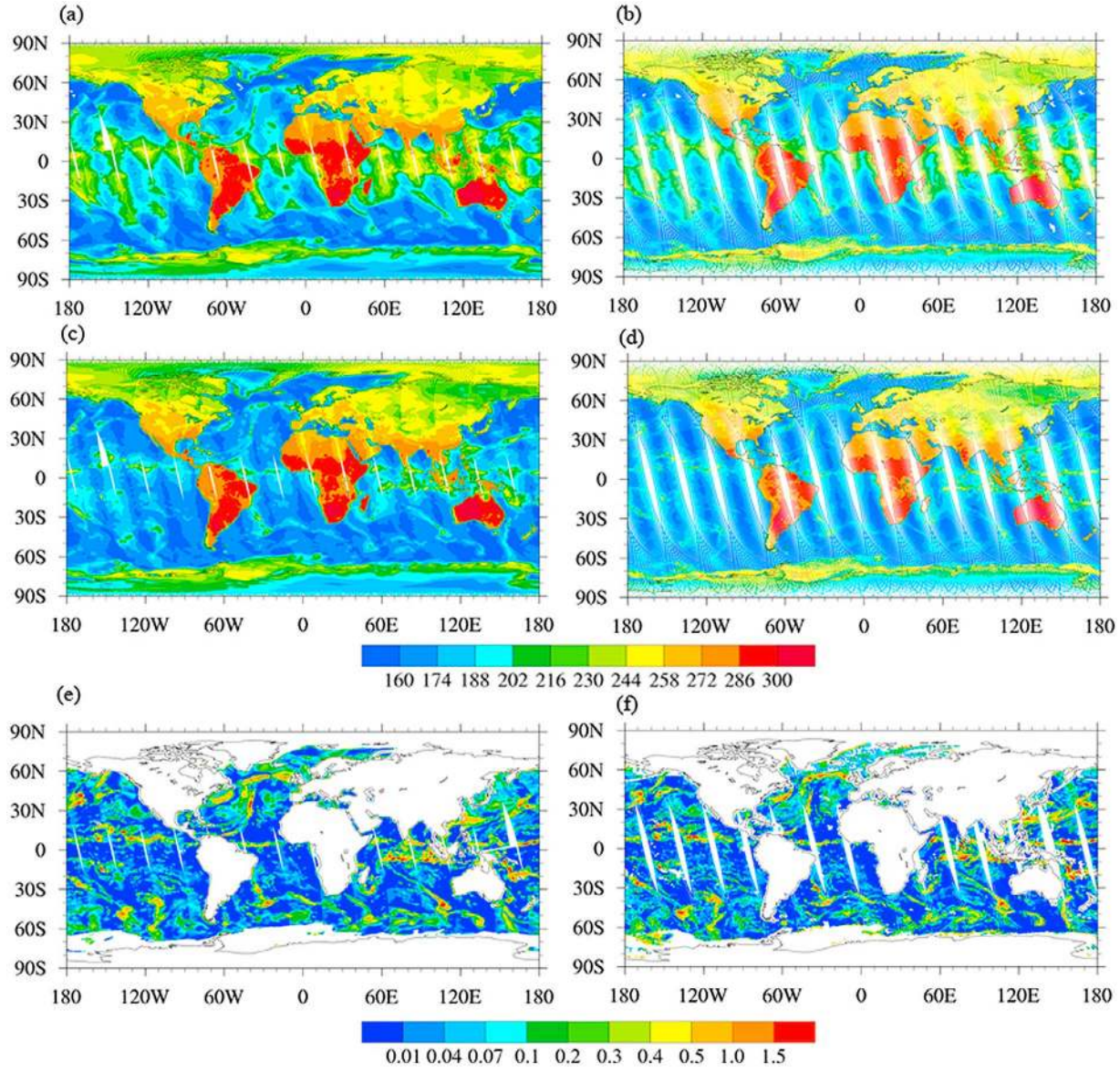

Figure 4. Brightness temperatures at (a and b) channel 1 and (c and d) channel 2, as well as (e and f) LWP retrievals over ocean from (left) ATMS and (right) AMSU-A from the ascending nodes on 20 December 2011.

are shown in Figure 6. It is shown that the original ATMS has a larger spread than the remapped data. This is due partially to higher channel noise, and partially to the fact that small-scale features of the real atmosphere which vary rapidly in time are not captured by the GFS fields and the averaging improves the agreement between satellite data and model simulations. It is noticed that the O-B data points within the same FOV number appear to increase with respect to the observed brightness temperature value (Figures 6a and 6c), but not with respect to the simulated brightness temperature, especially near the nadir. This is due to a larger variability in observations than that in model simulations, especially near the nadir where the peak WF altitude is the lowest for ATMS channel 6. The observed temperature range for the same FOV (Figures 6a and 6c) is larger than model simulation (Figures 6b and 6d). It is also noticed that observations for the ending half of the scan line (FOVs 49–96, Figures 6c and 6d) are more negatively biased than for the beginning half scan line (FOVs 1–48, Figures 6a and 6b).

[21] Figure 7 shows the biases and standard deviations of brightness temperatures for ATMS temperature sounding channels and the remapped data within [60S, 60N] under clear-sky conditions over ocean during 20–27 December 2011. It is reminded that biases in Figure 7(top) are not in the absolute sense, but are relative to the GFS model fields. Negative biases are found for ATMS channels 5–9 that are located within troposphere and low stratosphere, and positive biases are found for ATMS channels 10–14 in the stratosphere and higher. The highest channel 15 has a

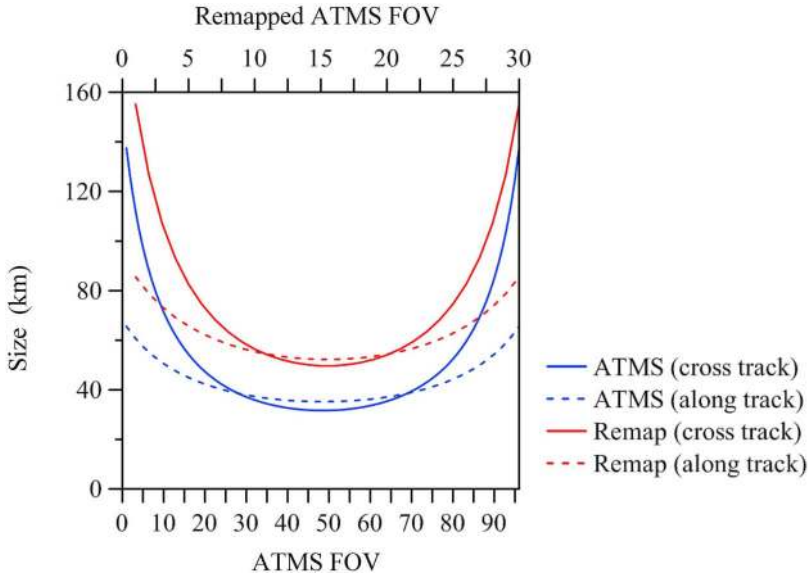

Figure 5. Cross-track (solid) and along-track (dashed) FOV size of ATMS (blue) and remapped (red).

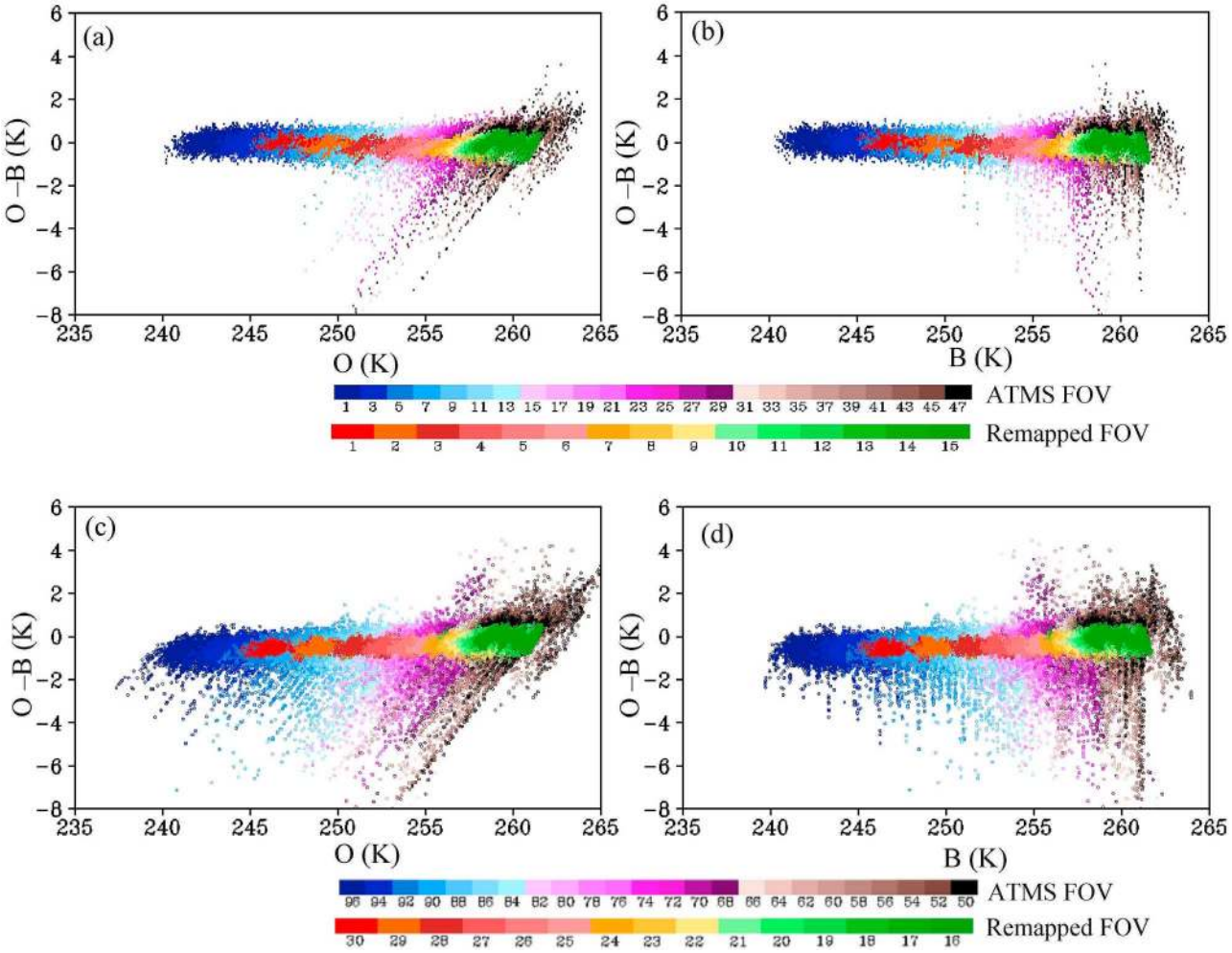

Figure 6. (a and b) Scatterplots of the temperature dependence of O-B for ATMS channels 6 with respect to the (left) observed and (right) modeled brightness temperatures at ATMS FOVs 1–48 (upper color bar) and ATMS remapped FOVs 1–15 (lower color bar) for all the data within 10S–10N on 20 December 2011. (c and d) Same as Figures 6a and 6b except for ATMS FOVs 29–96 and remapped FOVs 16–30.

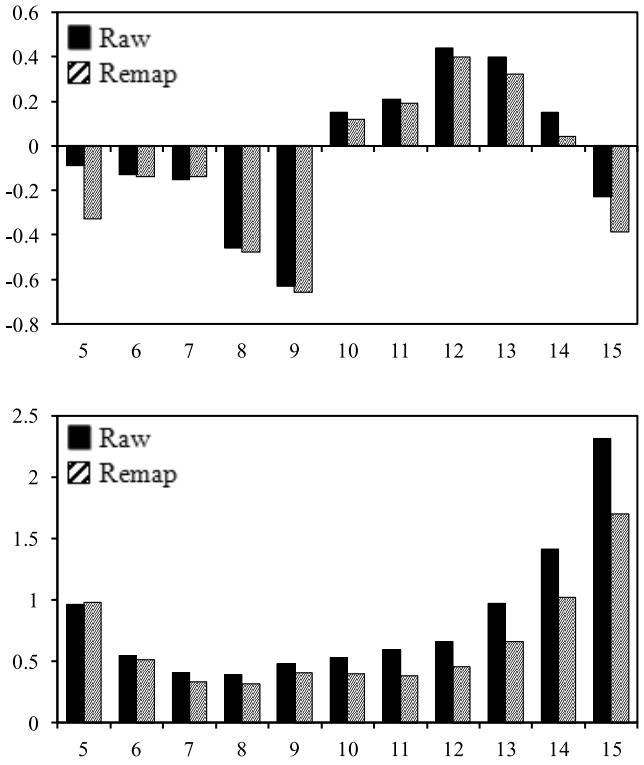

Figure 7. (top) Biases and (bottom) standard deviations of O-B brightness temperatures for ATMS temperature sounding channels with (dashed bar) and without (solid bar) remap for all the data within [60S, 60N] under clear-sky conditions over ocean during 20–27 December 2011.

negative bias. Impacts of remap on data biases are rather small (e.g., ≤0.1 K) except for channels 5 and 15 (~0.2–0.3 K). The remap does not change the sign of biases. The standard deviations of the remapped data are smaller than the ATMS raw data as expected, with a larger reduction of standard deviations for higher-level channels. An examination of the latitudinal dependence of bias and standard deviation (Figure 8) reveals that the biases of ATMS data in the middle and low troposphere (e.g., channels 5–7) are slightly higher at high latitudes than the middle and low latitude, and the reverse is true for the remaining upper level sounding channels except for channel 15. The standard deviation is larger for channels 14–15 at all latitudes and channel 5 in middle latitudes with high-terrain areas. The standard deviation is reduced at all latitudes after remapping.

[22] A unique feature of a cross-track scanning radiometer instrument is the so-called limb effect, which arises from the variation of the optical path length with scan angle. This limb effect is modeled through CRTM. Therefore, an a priori limb-adjustment is not required for ATMS data assimilation. However, the atmospheric inhomogeneity increases with scan angle, which may not be explicitly simulated in radiative transfer models. An obstruction to satellite observations by the spacecraft radiation may occur at large scan angles, which is usually difficult to be taken into account in the forward model and calibration process. Therefore, scan-angle dependent biases of both the observed brightness temperatures and those simulated from radiative transfer models are anticipated for cross-track scanning radiometer instruments. In many applications such as NWP radiance assimilation, angular-dependent biases between the observed brightness temperatures and those simulated from radiative transfer models must be quantified and be removed from data [*Harris and Kelly*, 2001; *Weng et al.*, 2003; *Zou et al.*, 2011].

[23] Figure 9 presents scan-dependent biases of ATMS channels 5–15 estimated separately for ascending and descending nodes. If the atmospheric inhomogeneity is the only source of biases, a symmetric bias distribution is expected. However, an asymmetric scan bias pattern is noticed for all ATMS channels examined. Channels 5–12 are more negatively biased near the ends of ATMS scanline, and channels 13–15 are more negatively biased at the starts of ATMS scanline toward a cold temperature. A temperature dependence of scan biases is noticed, evidenced by the different bias magnitudes for ascending and descending nodes of the same channel (e.g., channels 10–14) and the different bias magnitudes for different channels. This probably arises from the contributions from its near (e.g., spacecraft) and far field (e.g., Earth view) sidelobes. Further studies are needed for finding and confirming the root causes of the asymmetric bias pattern found for ATMS antenna temperatures using pitch maneuver data.

4. Tropical Depression Observed by ATMS

[24] Tropical cyclone Giovanna was formed over Southern Indian Ocean off the east coast of Madagascar. At 2200 UTC 12 February Giovanna reached Category-3 (Saffir-Simpson scale) hurricane intensity with a maximum sustained wind speed of 120 mph and a minimum sea level pressure of 930 hPa. Figure 10 shows the antenna temperatures of ATMS channels 3 and 18 from the descending node on 12 February 2012 around Hurricane Giovanna (Figures 10b and 10d). For comparison purposes, the antenna brightness temperatures of AMSU channels 3 and 20 from the descending node of NOAA-18 on the same day are also shown (Figures 10c and 10e). The National Centers for Environmental Prediction (NCEP) Final global analyses (FNLs) shows a low-pressure trough system with a value less than 1005 hPa (Figure 10a) over warm ocean surface and is located over a warm center of the ATMS channel 3 brightness temperature observations. The larger ocean surface emissivity at higher frequency makes the brightness temperature at 183.31 ± 7.0 GHz (channel 18) much warmer than that at 50.30 GHz (channel 3) outside the convective regions. The presence of cloud renders the brightness temperature at channel 3 warmer due to higher thermal emission from clouds (Figure 10a). In the convective region where the precipitation size ice particles are present, the brightness temperature at channel 18 is colder due to an increasing scattering. Notice that the orbital gap of AMSU-A/MHS is about 2.5 wider than that of ATMS. Brightness temperatures from the corresponding AMSU-A channels 3 and 20 (Figures 10c and 10e) compare favorably with ATMS observations except for a larger spacing between neighboring FOVs.

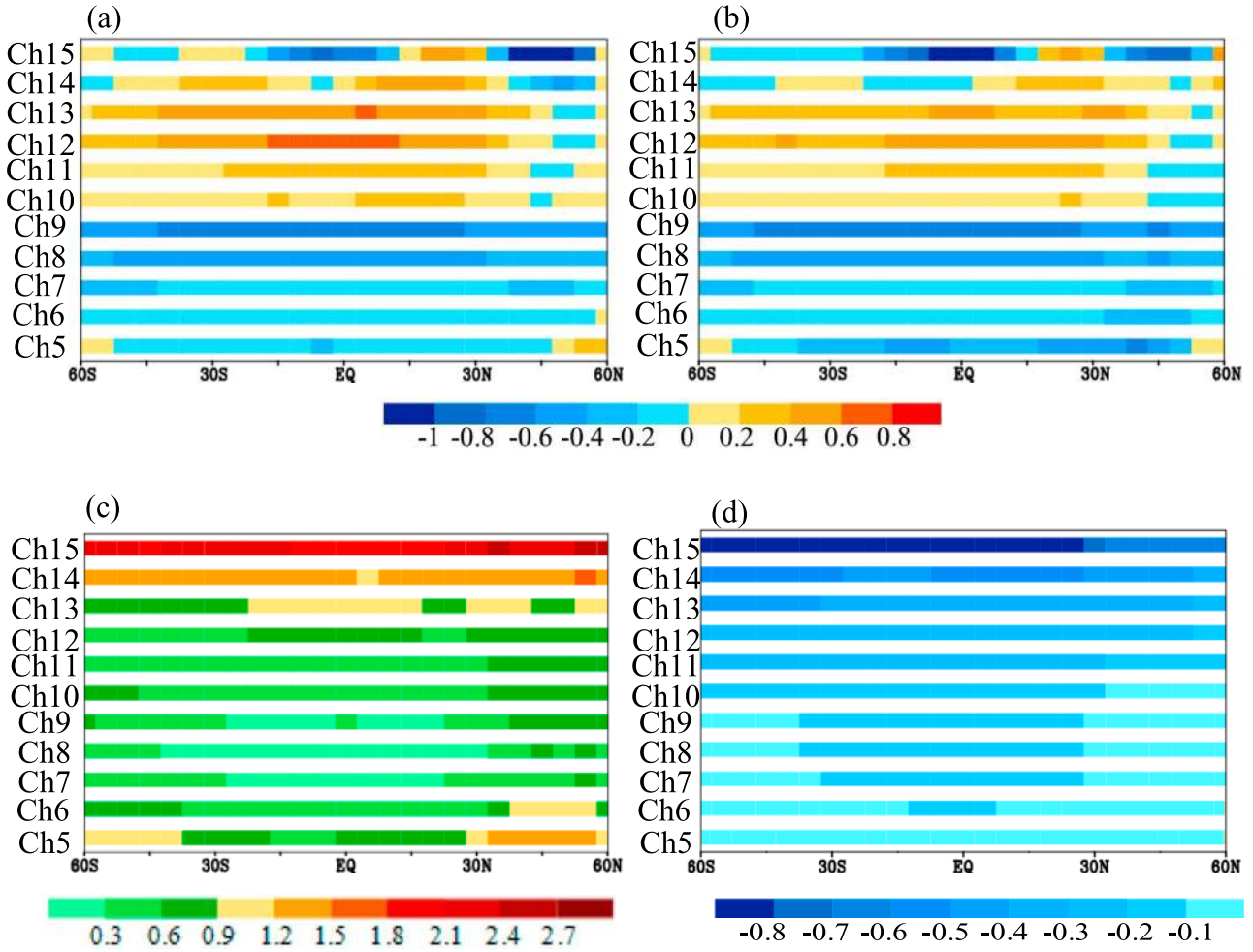

Figure 8. Latitudinal distributions of O-B biases for (a) ATMS raw data and (b) ATMS remapped data, (c) standard deviations for ATMS channels 5–15 (σ^2_{ATMS}), and (d) differences of σ^2_{ATMS} and the standard deviation for ATMS remapped data (σ^2_{remap}), i.e., $\sigma^2_{ATMS} - \sigma^2_{remap}$.

[25] Figure 11 shows two cross-sections of antenna temperatures for ATMS channels 3–7 (Figure 11a) and ATMS channels 17–22 (Figure 11b) along the black line in Figures 10b or 10d along the 72nd FOV of the ATMS swath shown. The temperature is as low as 233 K for ATMS window channel 3. ATMS channel 5 with its peak WF located at 850 hPa is warmest. A warm anomaly is found near the hurricane center for channels 3 and 4. For water vapor sounding channels 17–22 (Figure 11b), the eye of Hurricane Giovanna is characterized by a warm brightness temperature of similar magnitude as in Giovanna's environment for all six water vapor channels. The brightness temperatures in the eyewall are more than 100 K lower than those in the hurricane eye and its environment. The asymmetric structures of Hurricane Giovanna are fully captured by ATMS observations.

[26] Distributions of cloud LWP within and around Hurricane Giovanna are shown in Figure 12. Brightness temperatures of ATMS and NOAA-18 AMSU-A channels 1–2 during 1800 UTC to 2200 UTC 12 February 2012 are employed for the physical retrieval. The general pattern of cloud LWP distributions from both sensors compares favorably. The ability for the ATMS to enhance tropical cyclone structures with smaller ATMS footprints is highlighted in Figures 12c and 12d. A sharper radial gradient of LWP is found by the ATMS retrieval. A minimum LWP near the hurricane eye is present in the ATMS LWP (Figure 12c), but not in the AMSU-A retrieval (Figure 12d).

[27] ATMS channels 3–16 are located near 60 GHz along an oxygen absorption line. Microwave radiance at these channels is a linear function of the atmospheric temperature [*Janssen*, 1993] and responds to the thermal radiation at various altitudes because of their weighting function distributions (see Figure 2). Therefore, temperatures at a specified pressure level can be expressed as a linear combination of brightness temperatures measured at various sounding channels [*Kidder et al.*, 1978, 2000; *Grody*, 1979; *Zhu et al.*, 2002]. Following the work by *Zhu et al.* [2002], ATMS brightness temperatures at channels 5–16 and satellite local zenith angle are used as predictors for deriving temperature at a pressure level using the following regression equation:

$$T(p) = C_0(p) + \sum_i^n C_i(p) T_b(\nu_i) + C_{sz}(p) \frac{1}{\cos(\theta)}, \qquad (3)$$

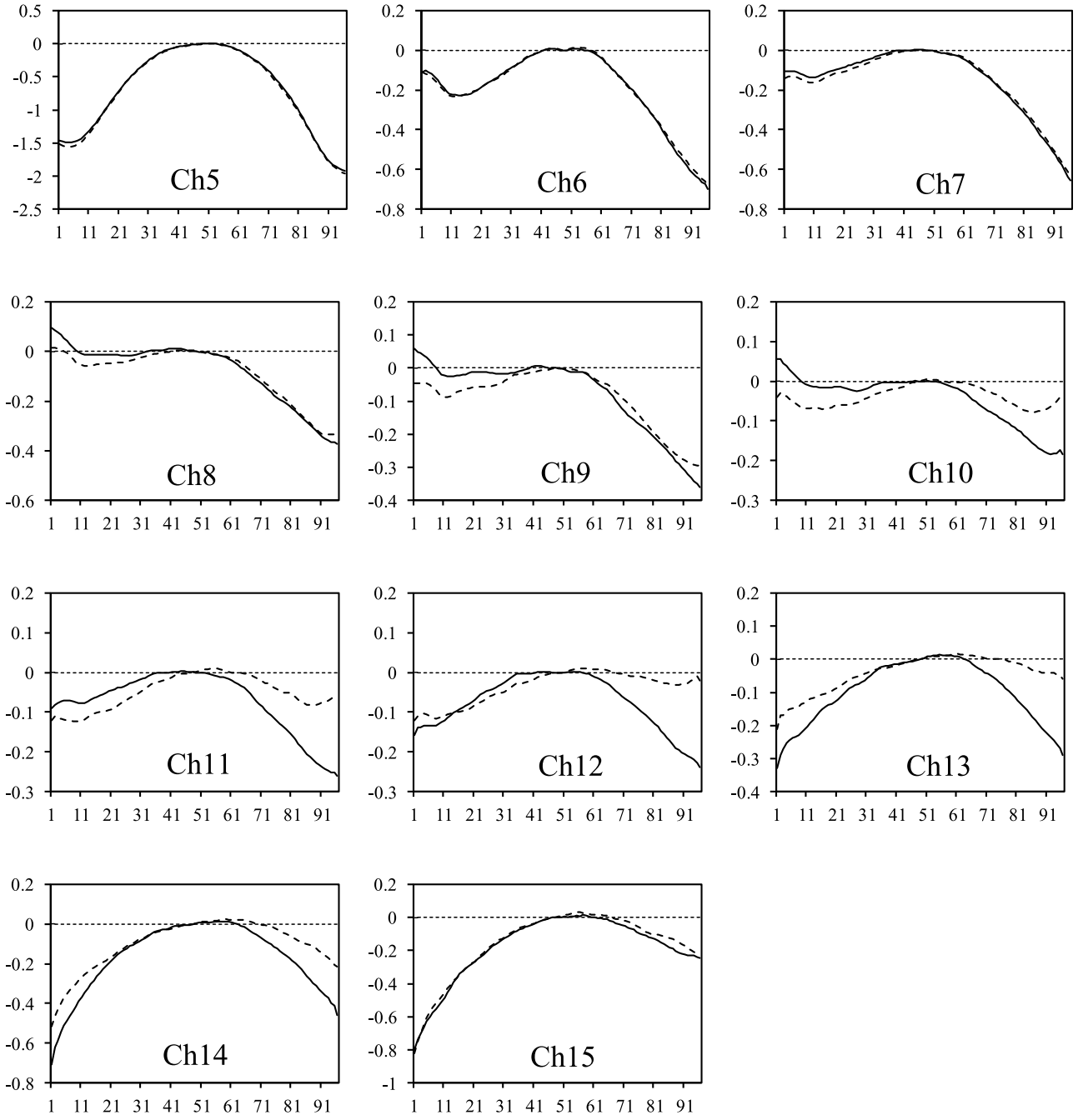

Figure 9. Scan-dependent biases of ATMS channels 5–15 at ascending (solid) and descending nodes (dashed) within [60S, 60N].

where p is the pressure level, θ is the satellite local zenith angle, v_i is the frequency at the *ith* channel, T_b is the ATMS brightness temperature, C_0, C_i, and C_{sz} are regression coefficients.

[28] The coefficients, C_0, C_i, and C_{sz}, are determined based on NCEP GFS model fields in clear-sky conditions over ocean within 60S and 60N. Since ATMS is a cross-track scanning instrument, the temperature retrieval at each pressure level is derived separately for each scanning angle. Figure 13 shows a vertical cross section of the temperature anomaly at the mature stage when Giovanna reached category-3 intensity. (The temperature anomaly is defined herein as a deviation from the unperturbed environmental temperature.) Apparently, a warm core can be identified in the upper troposphere with a maximum of about 12°C near 250 hPa. This anomaly structure is comparable to that found for Hurricane Bonnie (1998) at its category-3 intensity. However, an unrealistic 10°C negative anomaly is found in the lower and middle troposphere in the hurricane eyewall due to contamination by the thermal emission of large cloud droplets in

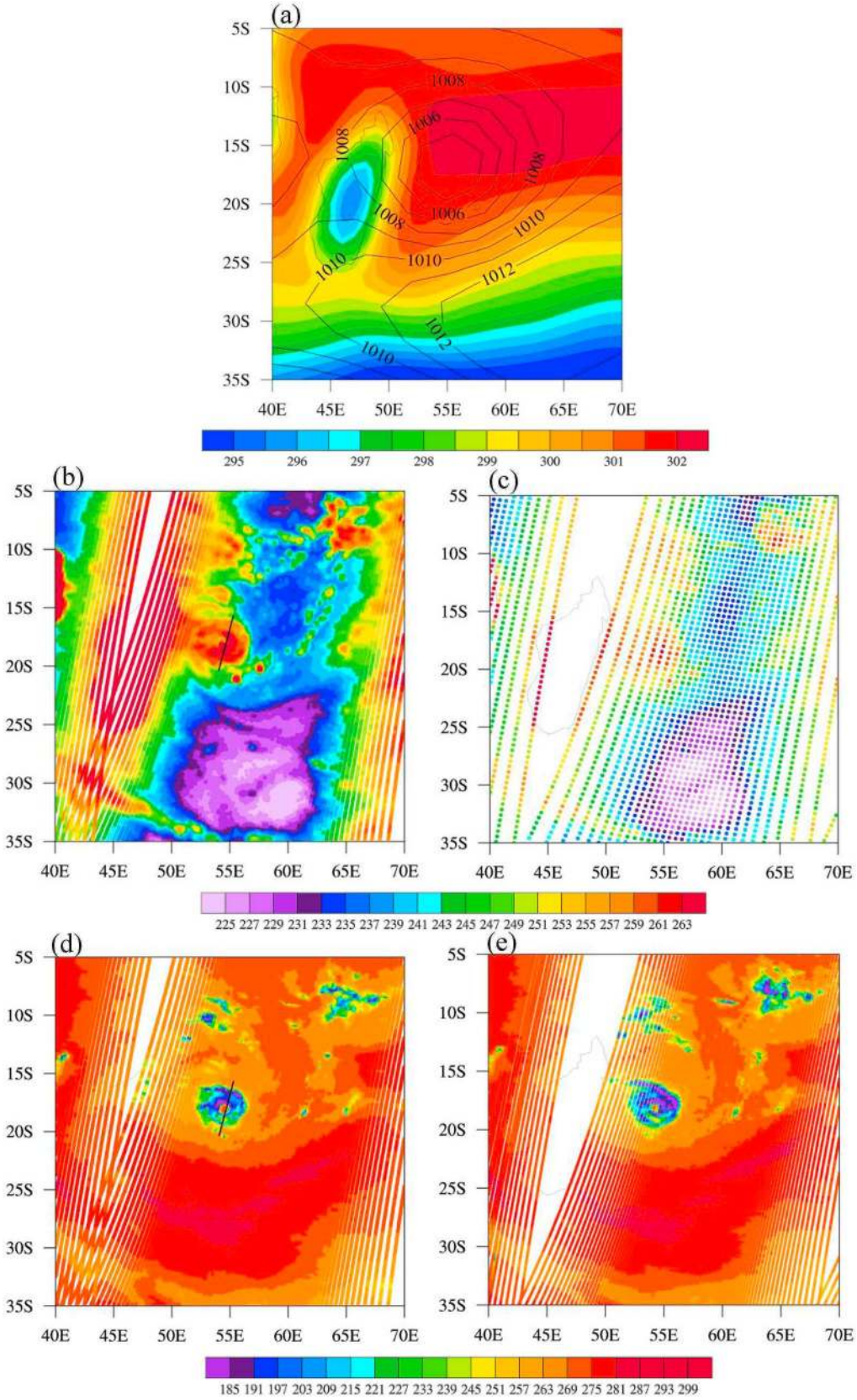

Figure 10. (a) Sea level pressure and sea surface temperature of NCEP FNL data at 1800 UTC 12 February 2012, as well as antenna temperatures at (b) ATMS channel 3 and (c) NOAA-18 AMSU-A channel 3, (d) ATMS channel 18, and (e) NOAA-18 AMSU channel 20 for the descending node 12 February 2012.

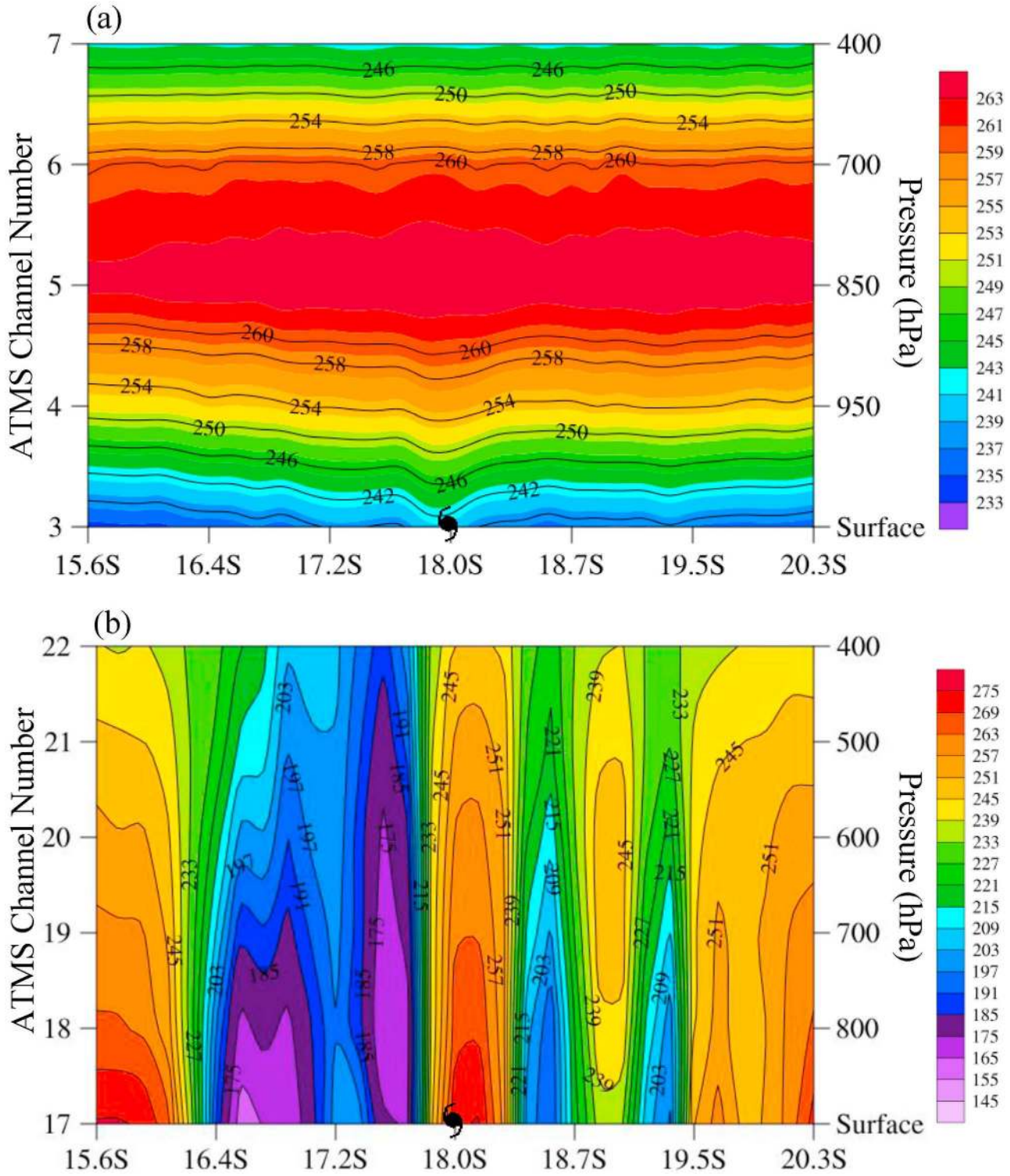

Figure 11. Cross sections of antenna temperatures for (a) ATMS channels 3–7 and (b) ATMS channels 17–22 along FOV72 (see the black line in Figure 10a).

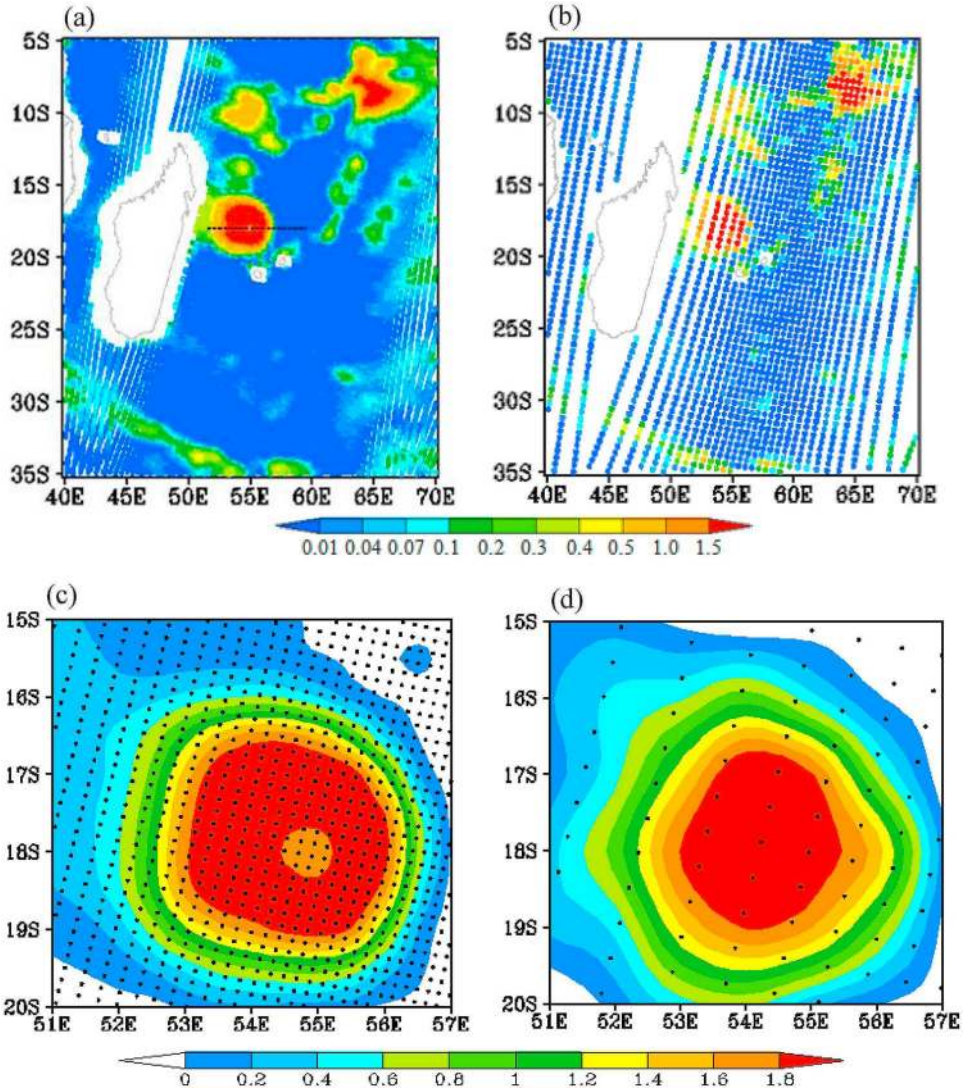

Figure 12. (a) ATMS and (b) NOAA-18 AMSU-A retrieval cloud LWP from 1800 UTC to 2200 UTC 12 February 2012. (c and d) Same as Figures 12a and 12b except for a zoomed area within hurricane Giovanna. The observation data points are indicated in Figures 12c and 12d by black dots.

heavy precipitation regions. Further investigation is required to remove the precipitation contamination.

5. Summary and Discussions

[29] There are increasing interests for enhanced satellite data assimilation efforts for improved tropical cyclone track, intensity and structure forecasts. The ATMS data over deep Atlantic and Pacific oceans are extremely valuable where the hurricane aircraft reconnaissance missions are usually not planned to those locations far from the coast. Since the ATMS scan angle ranges within ±52.77°, which is significantly larger than that of AMSU-A (e.g., ±48.33°), the ATMS provides data with no orbital gap poleward of 20° and also significantly reduces the unobserved regions within 20S–20N as demonstrated in this study. The three added new ATMS channels and the increased resolution of ATMS channels 3–16 (about 31.64 km at nadir) better resolves the tropical cyclone and convective precipitation structures than AMSU channels 3–15, which has a much coarser resolution of 47.46 km.

[30] Earlier microwave temperature and humidity sensors, the Microwave Sounding Unit (MSU) and the Advanced Microwave Sounding Unit (AMSU) have provided a rich heritage for ATMS. The MSU instruments onboard Tiros-N, NOAA-6 to NOAA-14 have four temperature channels and five water vapor channels and provided data from 1979 to 2006. The AMSU instruments onboard NOAA-15 to NOAA-19 added 11 more temperature channels to four MSU channels, giving a total of 15 temperature channels. AMSU channels 3, 5, 7 and 9 are similar to MSU channels 1–4. ATMS channels 3, 6, 8 and 10 are nearly the same as AMSU channels 3, 5, 7 and 8, respectively. ATMS has several important extensions and improvements relative to its predecessors. Many unique features of ATMS make its data most suitable for capturing detailed thermal structures for the improved monitoring and forecasting of tropical

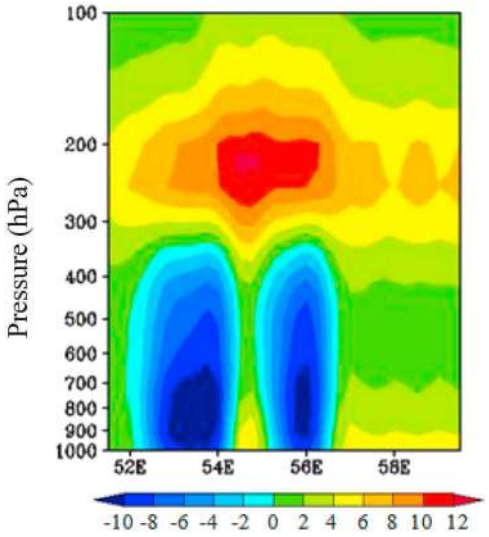

Figure 13. Vertical cross section of ATMS retrieved atmospheric temperature anomalies along the dashed line in Figure 12a.

cyclones. The new additions and modifications in channel frequency, resolutions, and swath width will allow better initialization and satellite data assimilation for tropical cyclones. By putting together MSU and the MSU-like AMSU and ATMS channels, a long-term series of global satellite microwave temperature sounding data of more than 30 years become available for studies of global climate changes. In doing so, microwave sounding instruments onboard weather satellites require a full characterization of their postlaunch accuracy and long-term stability. Our next task is to develop advanced algorithms for further quantification and removal of the errors of ATMS brightness temperatures contributed from various sources such as antenna spill-over effects and cross-polarization.

[31] **Acknowledgments.** The views expressed in this publication are those of the authors and do not necessarily represent those of NOAA. The third and fourth authors are supported by Chinese Ministry of Science and Technology project 2010CB951600. We thank Tong Zhu for generating the sounding retrieval and Ninghai Sun for providing ATMS data by Interface Data and Processing Segment (IDPS) through decoding.

References

Backus, G., and F. Gilbert (1968), The resolving power of gross earth data, *Geophys. J. R. Astron. Soc.*, *16*, 169–205, doi:10.1111/j.1365-246X.1968.tb00216.x.

Greenwald, T. J., G. L. Stephens, T. H. Vonder Haar, and D. L. Jackson (1993), A physical retrieval of cloud liquid water over the global oceans using Special Sensor Microwave/Imager (SSM/I) observations, *J. Geophys. Res.*, *98*, 18,471–18,488, doi:10.1029/93JD00339.

Grody, N. C. (1979), Typhoon "June" winds estimated from scanning microwave spectrometer measurements at 55.45 GHz, *J. Geophys. Res.*, *84*, 3689–3695, doi:10.1029/JC084iC07p03689.

Grody, N. C., J. Zhao, R. Ferraro, F. Weng, and R. Boers (2001), Determination of precipitable water and cloud liquid water over oceans from the NOAA-15 Advanced Microwave Sounding Unit (AMSU), *J. Geophys. Res.*, *106*, 2943–2953, doi:10.1029/2000JD900616.

Han, Y., F. Weng, Q. Liu, and P. V. Delst (2007), A fast radiative transfer model for SSMIS upper atmosphere sounding channel, *J. Geophys. Res.*, *112*, D11121, doi:10.1029/2006JD008208.

Harris, B. A., and G. Kelly (2001), A satellite radiance-bias correction scheme for data assimilation, *Q. J. R. Meteorol. Soc.*, *127*, 1453–1468.

Janssen, M. A. (1993), *Atmospheric Remote Sensing by Microwave Radiometry*, 572 pp., John Wiley, Hoboken, N. J.

Kidder, S. Q., W. M. Gray, and T. H. Vonder Haar (1978), Estimating tropical cyclone central pressure and outer winds from satellite microwave data, *Mon. Weather Rev.*, *106*, 1458–1464, doi:10.1175/1520-0493(1978)106<1458:ETCCPA>2.0.CO;2.

Kidder, S. Q., M. D. Goldberg, R. M. Zehr, M. DeMaria, J. F. W. Purdom, C. S. Velden, N. C. Grody, and S. J. Kusselson (2000), Satellite analysis of tropical cyclones using the Advanced Microwave Sounding Unit (AMSU), *Bull. Am. Meteorol. Soc.*, *81*, 1241–1259, doi:10.1175/1520-0477(2000)081<1241:SAOTCU>2.3.CO;2.

Kirsch, A., B. Schomburg, and G. Berendt (1988), The Backus-Gilbert method, *Inverse Probl.*, *4*, 771–783, doi:10.1088/0266-5611/4/3/014.

Poe, G. A. (1990), Optimum interpolation of imaging microwave radiometer data, *IEEE Trans. Geosci. Remote Sens.*, *28*, 800–810, doi:10.1109/36.58966.

Stogryn, A. (1978), Estimates of brightness temperatures from scanning radiometer data, *IEEE Trans. Antennas Propag.*, *26*, 720–726, doi:10.1109/TAP.1978.1141919.

Weng, F. (2007), Advances in radiative transfer modeling in support of satellite data assimilation, *J. Atmos. Sci.*, *64*, 3799–3807, doi:10.1175/2007JAS2112.1.

Weng, F., and N. C. Grody (1994), Retrieval of cloud liquid water using the Special Sensor Microwave Imager (SSM/I), *J. Geophys. Res.*, *99*, 25,535–25,551, doi:10.1029/94JD02304.

Weng, F., and N. C. Grody (2000), Retrieval of ice cloud parameters using a microwave imaging radiometer, *J. Atmos. Sci.*, *57*, 1069–1081, doi:10.1175/1520-0469(2000)057<1069:ROICPU>2.0.CO;2.

Weng, F., N. C. Grody, R. R. Ferraro, A. Basist, and D. Forsyth (1997), Cloud liquid water climatology derived from the Special Sensor Microwave Imager, *J. Clim.*, *10*, 1086–1098, doi:10.1175/1520-0442(1997)010<1086:CLWCFT>2.0.CO;2.

Weng, F., L. Zhao, R. Ferraro, G. Poe, X. Li, and N. Grody (2003), Advanced microwave sounding unit cloud and precipitation algorithms, *Radio Sci.*, *38*(4), 8068, doi:10.1029/2002RS002679.

Wentz, F. (1997), A well-calibrated ocean algorithm for Special Sensor Microwave Imager, *J. Geophys. Res.*, *102*, 8703–8718, doi:10.1029/96JC01751.

Zhu, T., D. Zhang, and F. Weng (2002), Impact of the advanced microwave sounding unit measurements on hurricane prediction, *Mon. Weather Rev.*, *130*, 2416–2432, doi:10.1175/1520-0493(2002)130<2416:IOTAMS>2.0.CO;2.

Zou, X., X. Wang, F. Weng, and G. Li (2011), Assessments of Chinese Fengyun microwave sounder (MWTS) measurements for weather and climate applications, *J. Atmos. Oceanic Technol.*, *28*, 1206–1227, doi:10.1175/JTECH-D-11-00023.1.